

RESEARCH ARTICLE

Genome-wide transcriptomics identifies an early preclinical signature of prion infection

Silvia Sorce¹, Mario Nuvolone^{1,2}, Giancarlo Russo³, Andra Chincisan¹, Daniel Heinzer¹, Merve Avar¹, Manuela Pfammatter¹, Petra Schwarz¹, Mirzet Delic¹, Micha Müller⁴, Simone Hornemann¹, Despina Sanoudou⁵, Claudia Scheckel^{1*}, Adriano Aguzzi^{1*}

1 Institute of Neuropathology, University of Zurich, Zurich, Switzerland, **2** Amyloidosis Research and Treatment Center, Foundation Scientific Institute Policlinico San Matteo, Department of Molecular Medicine, University of Pavia, Pavia, Italy, **3** Functional Genomics Center Zurich, ETH/University of Zurich, Zurich, Switzerland, **4** Institute of Molecular Life Sciences, University of Zurich, Zurich, Switzerland, **5** Clinical Genomics and Pharmacogenomics Unit, 4th Department of Internal Medicine, Attikon Hospital, Medical School, National and Kapodistrian University of Athens, Athens, Greece

* These authors contributed equally to this work.

* claudia.scheckel@usz.ch (CS); adriano.aguzzi@usz.ch (AA)



OPEN ACCESS

Citation: Sorce S, Nuvolone M, Russo G, Chincisan A, Heinzer D, Avar M, et al. (2020) Genome-wide transcriptomics identifies an early preclinical signature of prion infection. *PLoS Pathog* 16(6): e1008653. <https://doi.org/10.1371/journal.ppat.1008653>

Editor: Neil A. Mabbott, University of Edinburgh, UNITED KINGDOM

Received: May 18, 2020

Accepted: May 26, 2020

Published: June 29, 2020

Peer Review History: PLOS recognizes the benefits of transparency in the peer review process; therefore, we enable the publication of all of the content of peer review and author responses alongside final, published articles. The editorial history of this article is available here: <https://doi.org/10.1371/journal.ppat.1008653>

Copyright: © 2020 Sorce et al. This is an open access article distributed under the terms of the [Creative Commons Attribution License](https://creativecommons.org/licenses/by/4.0/), which permits unrestricted use, distribution, and reproduction in any medium, provided the original author and source are credited.

Data Availability Statement: All files are available from the GEO depository (accession number GSE144738). In addition, gene expression profiles during disease development can be easily

Abstract

The clinical course of prion diseases is accurately predictable despite long latency periods, suggesting that prion pathogenesis is driven by precisely timed molecular events. We constructed a searchable genome-wide atlas of mRNA abundance and splicing alterations during the course of disease in prion-inoculated mice. Prion infection induced PrP-dependent transient changes in mRNA abundance and processing already at eight weeks post inoculation, well ahead of any neuropathological and clinical signs. In contrast, microglia-enriched genes displayed an increase simultaneous with the appearance of clinical signs, whereas neuronal-enriched transcripts remained unchanged until the very terminal stage of disease. This suggests that glial pathophysiology, rather than neuronal demise, could be the final driver of disease. The administration of young plasma attenuated the occurrence of early mRNA abundance alterations and delayed signs in the terminal phase of the disease. The early onset of prion-induced molecular changes might thus point to novel biomarkers and potential interventional targets.

Author summary

Prion diseases are brain disorders caused by infectious proteins called prions. These diseases feature a long asymptomatic incubation phase which can last several years, followed by a phase of rapidly progressing mental deterioration that can lead to death within just few months. The mechanisms underlying the long incubation phase are elusive, impeding early diagnosis and limiting potential therapeutic interventions. In experiments, prion-infected mice develop the disease following a timeline similar to that of human prion diseases. Here we have studied gene expression at different time points during the development of disease in mice. Our results indicate that robust molecular changes can be

visualized and downloaded at the following website: <https://histodb12.usz.ch/iMice/public/PrionDatabase/PrionDatabase.php>.

Funding: A.A. is the recipient of an Advanced Grant of the European Research Council (670958), the Swiss National Foundation (179040, 183563), the Clinical Research Priority Programs “Small RNAs” and “Human Hemato-Lymphatic Diseases”, the Nomis Foundation and a donation from the estate of Dr. Hans Salvisberg. S.S. is recipient of a grant from the Synapsis foundation. M.N. is recipient of a grant from the Amyloidosis Foundation. C.S. was supported by a Marie Curie Individual Fellowship (706138). The funders had no role in study design, data collection and analysis, decision to publish, or preparation of the manuscript.

Competing interests: The authors declare that they have no conflict of interest.

detected much earlier than previously anticipated, months before mice begin to show clinical signs or brain tissue damage. Several months later, a reaction of glial cells heralds the overt clinical manifestations of disease. Experimental treatment aimed at “rejuvenating” mice prevents the early molecular changes and seems to impact on the subsequent later disease progression. Although therapies for prion diseases are still lacking, our data redefine the disease stages from a molecular perspective and might contribute to devise better-timed and potentially more efficacious interventions.

Introduction

After the onset of clinical signs, prion diseases typically progress very rapidly to a terminal stage, which is characterized by micro- and astrogliosis, vacuolation and neuronal loss. Sporadic Creutzfeldt-Jakob disease (CJD), the most common human prion disease, can lead to death within months of symptom onset[1]. Conversely, prion infections are often characterized by very long incubation times: iatrogenic cases of CJD after administration of prion-contaminated growth hormone display incubation times of >20 years[2] and Kuru, an acquired form of prion disease, was reported to arise decades after consumption of contaminated materials[3]. The extraordinary duration of the latency phase has led to the presumption that CJD may be caused by a “slow virus”. Although this hypothesis was dismissed[4], prion pathogenesis is initially insidious and only acquires a rapid rate of progression in the late stages of disease.

The seemingly incongruous combination of a very long latency and a rapidly progressing clinical disease can be reproduced in mouse models of prion infection[5]. After inoculation of prion-containing brain homogenate, wild-type mice experience an incubation period of several months followed by rapidly progressive neurological dysfunction. It was suggested that prion replication occurs without causing any neuronal damage until a plateau level of infectious particles is reached, whereas neurotoxicity arises because of a toxic form of PrP named “PrP^L”[6–8]. However, no physical evidence for the existence of “PrP^L” has ever come forth, and these experimental observations can be explained by alternative models. For example, small numbers of prion seeds may cause early molecular alterations that elicit late-onset clinical signs. This question may be addressed by creating longitudinal maps of the transcriptional equivalents of neurotoxicity from the administration of prions to the development of terminal disease.

Transcriptional maps of prion-inoculated mice were previously performed using microarrays[9–12], and more recently also by RNA sequencing (RNAseq)[13]. Most of these studies analyzed whole-brain homogenates and have focused on alterations occurring in the late phase of the disease. Yet no antiprion compounds could reverse the progression of disease[14], perhaps because intervention was too late. Instead, focusing on the preclinical changes occurring in the affected brain may uncover alternative targets for early diagnosis and therapeutic intervention in pre-symptomatic subjects. Here we performed a comprehensive analysis of transcriptional alterations in the hippocampus of prion-infected mice over time. We identified an unexpected wealth of PrP-dependent changes in the early phase of prion replication, long before any clinical signs of disease. Neuronal expression changes became evident only at the terminal stage of the disease, whereas the appearance of clinical symptoms coincided with microglia alterations. Prion-induced molecular changes were largely unaffected by ageing, yet the administration of young plasma attenuated early prion-induced changes and improved the health span of diseased mice.

Results

Identification of mRNA expression changes during prion disease

To identify molecular alterations associated with the progression of prion disease, we administered intracerebrally RML6 prions or non-infectious brain homogenate (NBH, for control) to wild-type C57BL/6J mice (Fig 1A). Mice were sacrificed at 4, 8, 12, 14, 16, 18 and 20 wpi (weeks post inoculation), as well as the terminal stage (the last time point during disease progression when mice can be humanely euthanized). We specifically focused on the hippocampal region. The hippocampus plays a central role in memory formation and consolidation and is one of the most affected and therefore most studied regions during prion disease[15]. RNA from ipsi- and contralateral hippocampi was extracted and subjected to RNA sequencing ($n = 3$ per prion and control samples at each time point except for two control samples at 20 wpi; S1 Table and S2 Table). All gene expression profiles during disease progression can be visualized and downloaded at [PrionRNAseqDatabase](#).

Hierarchical clustering analysis of total transcriptomes revealed a progressive segregation of prion-inoculated and control mice starting at 18 wpi (S1 Fig). However, principal component analysis (PCA) showed a separation of the two groups already at 8 wpi (S1 Fig). Next, we identified 3,723 differentially expressed genes (DEGs) between prion-infected and control mice (absolute \log_2 fold changes $|\log_2FC| > 0.5$ and false discovery rate (FDR) < 0.05 at least at one of the time points; Fig 1A and 1B; S3 Table). Consistent with the hierarchical clustering and the PCA, 813 genes changed at 8 wpi and the number of DEGs gradually increased during the later timepoints (Fig 1A).

Unsupervised kmeans clustering ($k = 4$ clusters; \log_2FC with $p \geq 0.05$ were set to 0) identified mRNAs with distinct expression patterns during disease progression (Fig 1B; only \log_2FC with $p < 0.05$ are colored). The clusters were further visualized with a t-distributed stochastic neighbor embedding (t-SNE) of the \log_2FC (Fig 1C; \log_2FC with $p \geq 0.05$ were set to 0). Clusters 1 and 3 correspond to genes that increase or decrease at the terminal stage only. In contrast, cluster 2 genes started to increase already at 16–18 weeks, and genes in cluster 4 showed an oscillating pattern, decreasing at 8 wpi, 16 wpi and the terminal stage, but recovering in between. Intersecting our data with an atlas of the most enriched transcripts in neurons (N), microglia (MG), astrocytes (AS), oligodendrocytes (OL) and vascular cells (VC)[16], revealed that the different clusters are populated by distinct cell types. While clusters 2 and 3 consist predominantly of microglia and neuronal genes, respectively, clusters 1 and 4 contain genes enriched in multiple cell types (Fig 1D and S2 Fig). This observation is further substantiated by heatmaps of genes distinctive to just one cell type (S2 Fig). Neuronal genes almost exclusively belonged to clusters 3 and 4, and corresponded to decreasing genes, whereas microglia genes were essentially all increasing and were contained in clusters 1 and 2. At the terminal stage, these patterns may partly reflect shifts in the cellular composition of the brain, with both microglia activation and neuronal loss being hallmarks of prion disease.

mRNA expression changes become evident in the early disease phase

The most conspicuous gene expression changes arose at the terminal time point ($|\log_2FC| > 0.5$ and $p < 0.05$), yet almost half of DEGs were shared between two or more time points (S2 Fig). Multiple patterns of gene expression changes became already evident in the cluster analysis (Fig 1B). To identify monotonic gene expression patterns, we selected terminal DEGs showing a consistent trend ($|\log_2FC| > 0.5$ and p value < 0.05) at consecutive time points. Of 1,872 terminally upregulated DEGs, 1, 87, 440 and 632 genes started to be monotonically upregulated at 14, 16, 18, and 20wpi, respectively. Conversely, of 1,081 downregulated DEGs, only 0,

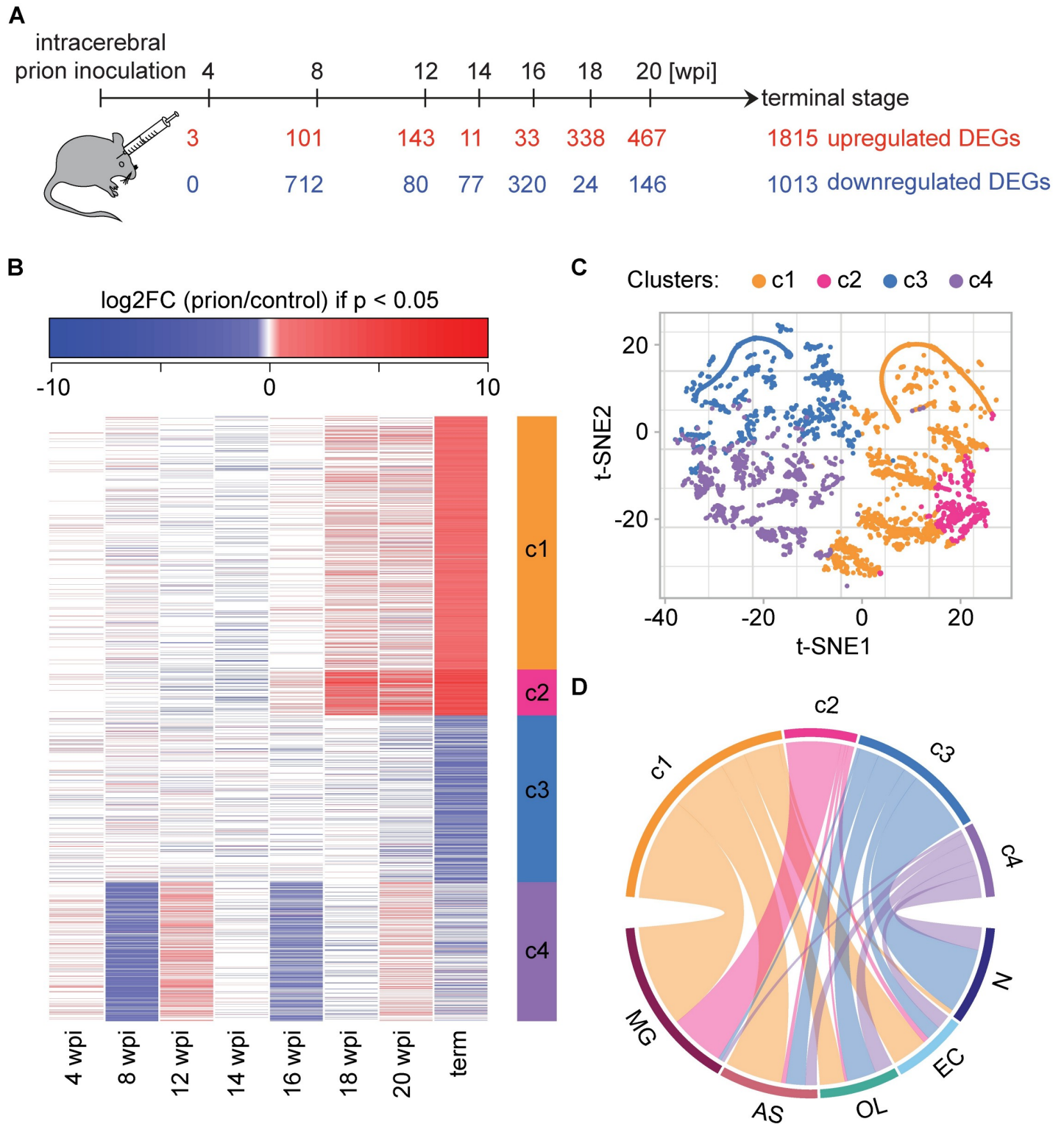


Fig 1. Identification of differentially expressed genes (DEGs) during prion disease progression. **A** Timeline of prion inoculations. Numbers of upregulated and downregulated DEGs ($|\log_2FC| > 0.5$ and $FDR < 0.05$) are indicated. Several DEGs were up- and downregulated at different time points. **B** Heatmap displaying the \log_2FC of 3,723 genes that are differentially expressed ($|\log_2FC| > 0.5$ and $FDR < 0.05$) at least at one time point. Only \log_2FC values with $p < 0.05$ are colored. Unsupervised kmeans clustering ($k = 4$ clusters) identified four coherent patterns (c1-c4) of \log_2FC oscillations over time (right side bar). **C** t-distributed stochastic neighbor embedding (t-SNE) plot (n components = 2, perplexity = 50) visualizing the separation of DEGs into four clusters. **D** Circos plot summarizing the cell type-enriched genes within each cluster. Clusters are identified by the same colors in panels b-d.

<https://doi.org/10.1371/journal.ppat.1008653.g001>

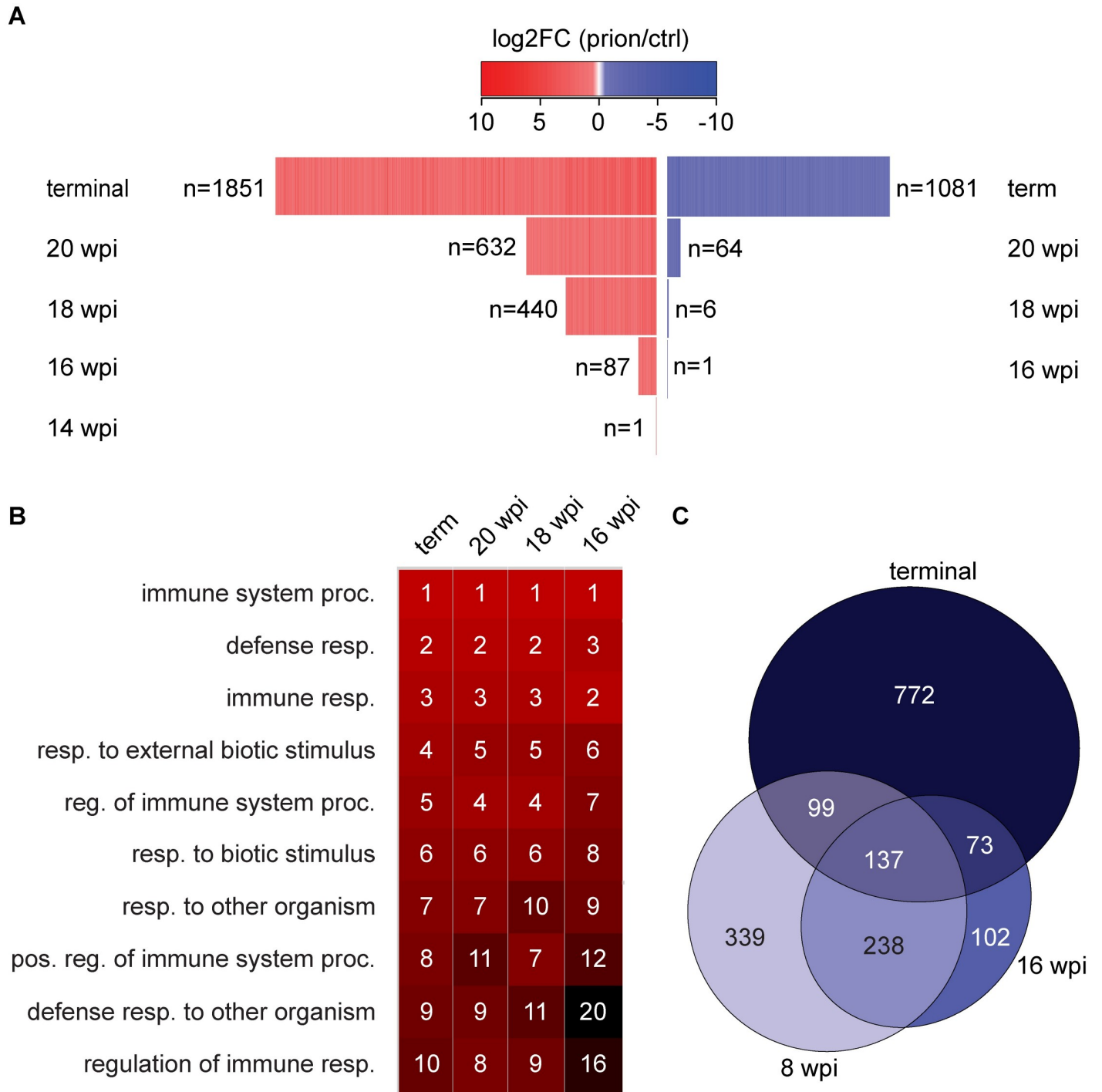


Fig 2. Consistent mRNA expression changes become evident in the early disease phase. **A** Heatmap displaying the \log_2FC of monotonic DEGs (mDEGs), defined as genes changing with a similar trend ($|\log_2FC| > 0.5$ and $p < 0.05$) at consecutive time points until terminal disease. n: number of mDEGs at each time point. **B** Heatmap displaying the top 10 GO terms enriched among terminally upregulated genes and their enrichment in mDEGs at 20, 18 and 16 wpi. Number and colors represent the ranking (high = red, black = low) of the respective GO terms. **C** Overlap of downregulated genes at 8 wpi, 16 wpi and at the terminal stage.

<https://doi.org/10.1371/journal.ppat.1008653.g002>

1, 6, and 64 genes showed a continuous decrease at those time points (Fig 2A). This illustrates that a monotonic pattern is specific to upregulated genes and becomes evident at 16wpi.

We further analyzed if these monotonic DEGs (mDEGs) were enriched for certain cell types. Consistent with the cluster analysis, upregulated mDEGs consisted mostly of microglia-enriched and to a lesser extent astrocyte-enriched transcripts (S2 Fig). Moreover, we found that the top enriched GO terms in terminally upregulated genes were shared between mDEGs at 20, 18 and 16 wpi (Fig 2B; S4 Table). GO terms related to vacuolation (a defining hallmark of prion diseases) started to be enriched at 18 wpi (S5 Table). Both microgliosis and vacuolation are characteristics of prion disease. Our data illustrates that both characteristics also become evident on the RNA expression level, months prior to the terminal stage of the disease. A further feature of human prion diseases is the profound loss of neurons. Yet only a minority ($n = 64$) of the 1081 terminally downregulated DEGs decreased already at 20 wpi (S2 Fig), and GO terms related to ion channels, synaptic transmission and neuron projection were only enriched among terminally downregulated DEGs (S6 Table).

We further focused on the oscillating DEGs associated with cluster 4 genes and assessed the overlap between genes downregulated at 8 wpi, 16 wpi and the terminal stage. 813 DEGs showed a decrease (with $p < 0.05$) already at 8 wpi although neither clinical nor histological changes are detectable at this time point (see below). The 813 genes showed a minor enrichment of neuronal genes (S2 Fig) and were characterized by GO terms related to extracellular matrix, cell adhesion and neuronal projection (S7 Table). Furthermore, a striking ~60% and ~80% of the 8 and 16-wpi decreasing genes, respectively, overlapped with each other or the terminally downregulated genes (S2 Fig). Interestingly, the initial downregulation at the 8- and 16-week timepoints was transient, indicating that compensatory mechanisms might act during the earlier stages of prion disease.

To validate these changes, we analyzed the 8 wpi and terminal time point in a second, validation cohort of mice, which were inoculated and analyzed independently from the first cohort (S3 Fig and S5 Fig). Consistently, we observed that cluster 4 genes (oscillating genes) decreased at 8 wpi and the terminal stage, and that cluster 3 genes (mainly neuronal genes) decreased at the terminal stage. Furthermore, genes belonging to clusters 1 and 2 increased at the terminal stage (S3 Fig). The 8 wpi changes do not occur in genes enriched in microglia, and we did not observe any differentially expressed genes shortly after prion inoculation at 4 wpi. These results suggest that the 8 wpi changes are not linked to an acute immune response in the brain due to the intracerebral inoculation. To further support this, we have analyzed intracerebrally inoculated C57BL/6J coisogenic PrP knockout mice at 8 wpi, and intraperitoneally inoculated C57BL/6J wild-type mice at 8 wpi and the terminal time point (S4 Fig and S5 Fig). Intracerebrally inoculated PrP knockout mice did not show any significant gene expression changes at 8 wpi (S4 Fig) indicating that the 8wpi changes in wild-type mice are not linked to intracerebral inoculations and importantly, are PrP-dependent. In contrast, intraperitoneally inoculated wild-type mice displayed a decrease in cluster 4 genes (S4 Fig; $p = 3.7e-30$), albeit at a lower level due to the slower disease progression associated with intraperitoneal prion administration. The terminal prion-induced changes were very similar between intracerebrally and intraperitoneally inoculated mice (S4 Fig and S5 Fig). Collectively, our data shows that hundreds of genes are downregulated at a very early disease stage in a PrP-dependent manner, suggesting that this early response is linked to primary pathogenic events rather than reactive changes.

Microglia activation drives symptomatic prion disease progression

We next aimed at correlating the gene expression changes with the progression of neuropathological changes. Mice reached the terminal stage of the disease at 170–180 days, at which point

they were sacrificed (median survival: 176 days; [S6 Fig](#)). Brain sections of prion-inoculated mice were assessed for morphological changes (haematoxylin/eosin), for astro- and microgliosis (GFAP and IBA1 staining) and for the presence of protease-resistant prion protein (PrP^{Sc}; protease treatment followed by SAF84 staining). PrP^{Sc} started to accumulate already at 12 wpi, whereas spongiosis, astro- and microgliosis became only evident after 16 wpi ([S6 Fig](#)). These results are in line with the transcriptomic data discussed above, which revealed that microglia-enriched genes started to increase at 16 wpi.

We next determined the concentration of prion propagons using a quaking assay. We found that the lag phase of the assay, which measures templated nucleation of PrP fibrils, continually decreased during disease progression ([S7 Fig](#)), suggesting that the amounts of infectious units increased up to the terminal stage. In parallel, we analyzed prion infectivity using the scrapie cell assay in endpoint dilution format, which yielded similar results as the quaking assay and confirmed that infectivity continuously increased from 8 wpi to the terminal stage. Prion titers were significantly higher at the terminal stage compared to 16 wpi ([S7 Fig](#)), which is in contrast to previous reports stating that infectivity would reach a plateau at 16 wpi[7].

To relate gene expression changes to neurological dysfunction, we assessed the motor performance of prion-inoculated and control mice using a rotarod test. We observed a progressive decline in motor performance starting at 18 wpi ([Fig 3A](#)), which became significant at 19 wpi. The onset of impairment was synchronous to increased expression of microglia-enriched genes and was unlinked to decreased expression of neuronal genes which became evident only at the terminal stage ([Fig 3B](#)). A linear regression analysis between rotarod performance and the expression change of each of the 3723 DEGs, identified a significant correlation for 347 DEGs ($p < 0.001$). Examples of correlated non-enriched, microglia-enriched and neuronal-enriched genes are shown ([Fig 3C](#)). While the linear regression slope of microglia genes was negative, neuronal genes exhibited a positive linear regression slope. This was confirmed when we compared the average slope between DEGs enriched in different cell types ([Fig 3D](#)). We conclude that motor decline, neuropathological changes and an increase in microglia gene expression occur simultaneously, long before terminal changes in neuronal gene expression and neuronal loss become evident. This suggests that microglia, rather than neurons, could be the final drivers of prion disease progression. However, the transcriptional changes observed at 8 wpi precede both the onset of clinical signs and any changes in microglial gene expression, suggesting they are independent of any changes of microglial states. The early 8 wpi changes might thus hierarchically control microglia changes and ultimately induce pathogenesis.

Identification of post-transcriptional changes during prion disease progression

Many RNA binding proteins are exclusively expressed in neurons, and aberrant splicing has been linked to multiple neurodegenerative diseases[17]. We identified a total of 426 isoforms that were differentially expressed in prion-inoculated mice at one or more time points ($FDR < 0.05$; [Fig 4A](#); [S8 Fig](#)). 102 of these splice isoforms mapped to DEGs, indicating that differential splicing of these transcripts might impact their abundance ([S8 Fig](#)). The 426 isoforms correspond to 239 splicing events, which mapped to 228 genes. Most of these genes showed just one significantly changing splicing event, except *App*, *Chl1*, *Evl*, *Fus*, *Neo1*, *Olfm1*, *Picalm*, *Ppfia4* and *Sorbs1*. The majority of splicing changes consisted of exon inclusion/skipping followed by alternative transcript starts/ends ([Fig 4B](#)). And while most splicing changes occurred only at the terminal stage, many splicing events showed a similar trend ($p < 0.05$) at multiple time points during disease progression. Most strikingly, we observed an oscillating pattern of isoform expression at 8 wpi, 16 wpi and the terminal stage ([Fig 4C](#)), indicating that these time-points are marked by a characteristic RNA expression and splicing signature.

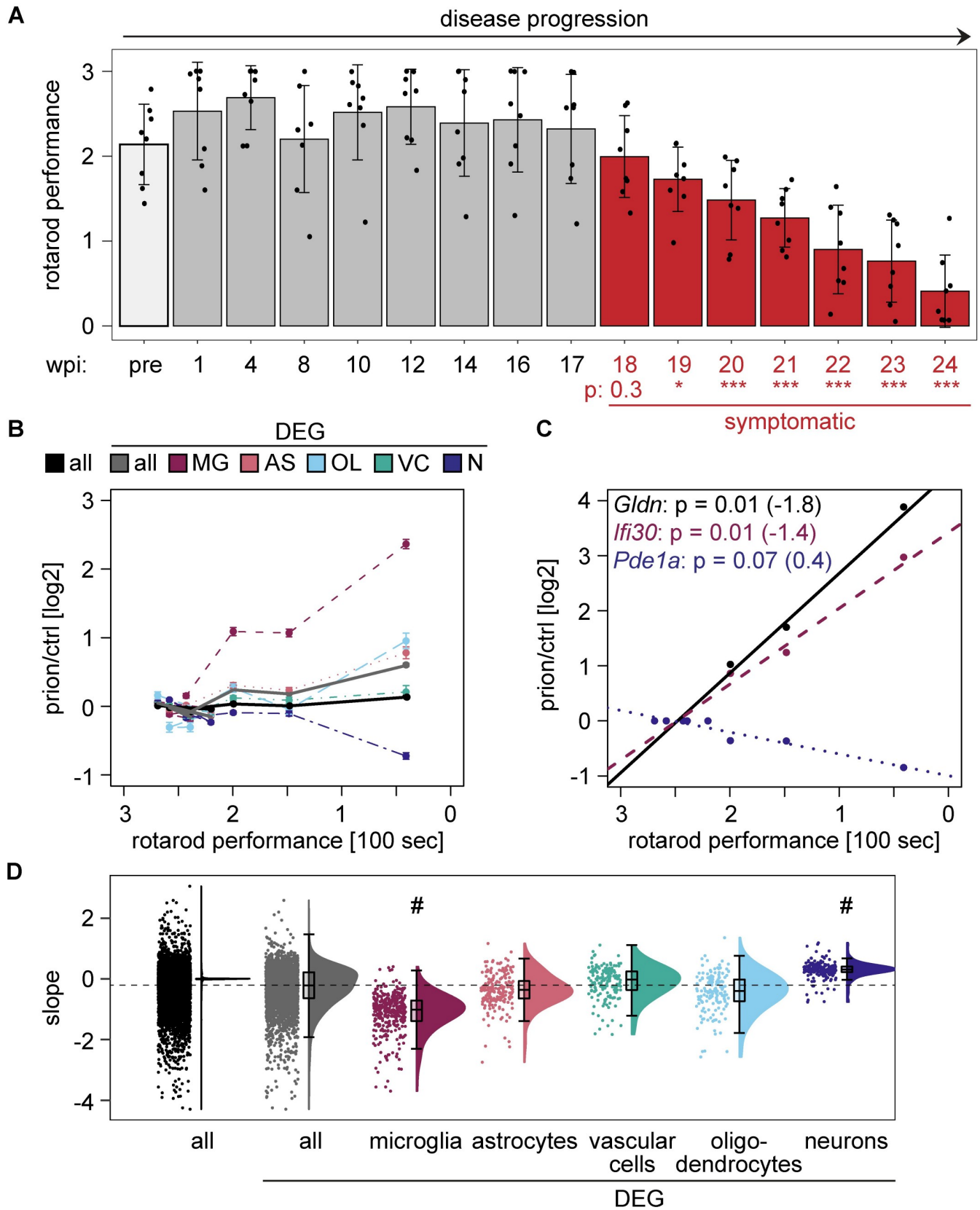


Fig 3. Microglia activation and prion disease progression. **A** Rotarod performance of prion-inoculated mice during disease progression (pre = pre-inoculation). Bars represent the mean latency to fall in 100 seconds. Each dot represents one individual mouse. P-adjusted: P values were calculated with a one-way ANOVA followed by Tukey’s multiple comparison test (* $p < 0.05$; *** $p < 0.001$; compared to 1 wpi). Red: symptomatic phase of disease. Error bars: standard deviation. **B** Comparison of rotarod performance (latency to fall in 100 seconds) and average \log_2FC at the corresponding time point. Lines represent all genes, all DEGs or DEGs that are enriched in the indicated cell type. Error bars: standard error of the means (SEM). **C** Linear regression analysis between the rotarod performance and the gene expression changes of individual genes. Shown are the most significantly correlating genes that were non-enriched (black), microglia-enriched (red-violet) and neuronal-enriched (violet-blue). Corresponding Bonferroni-corrected p values and slopes of the linear regression analysis are indicated in brackets. **D** Raincloud plot displaying the slope distribution of the linear regression analysis. The slope between all DEGs and DEGs that are either microglia- or neuron-enriched differs significantly ($p < 1 \times 10^{-14}$; one-way ANOVA followed by Tukey’s multiple comparison test).

<https://doi.org/10.1371/journal.ppat.1008653.g003>

Select differentially spliced isoforms are shown in **S8 Fig** (indicated in **S8 Table**). Skipping of exon 17 of *Picalm*, a susceptibility gene for late-onset Alzheimer’s disease[18] was increased at the terminal stage of prion disease. Skipping of exon 17 introduces a premature stop codon, which leads to the production of a truncated protein, and is thought to affect clathrin-mediated synaptic endocytosis[19,20]. The inclusion of exons 7 and 8 of *App*, a well-described splicing

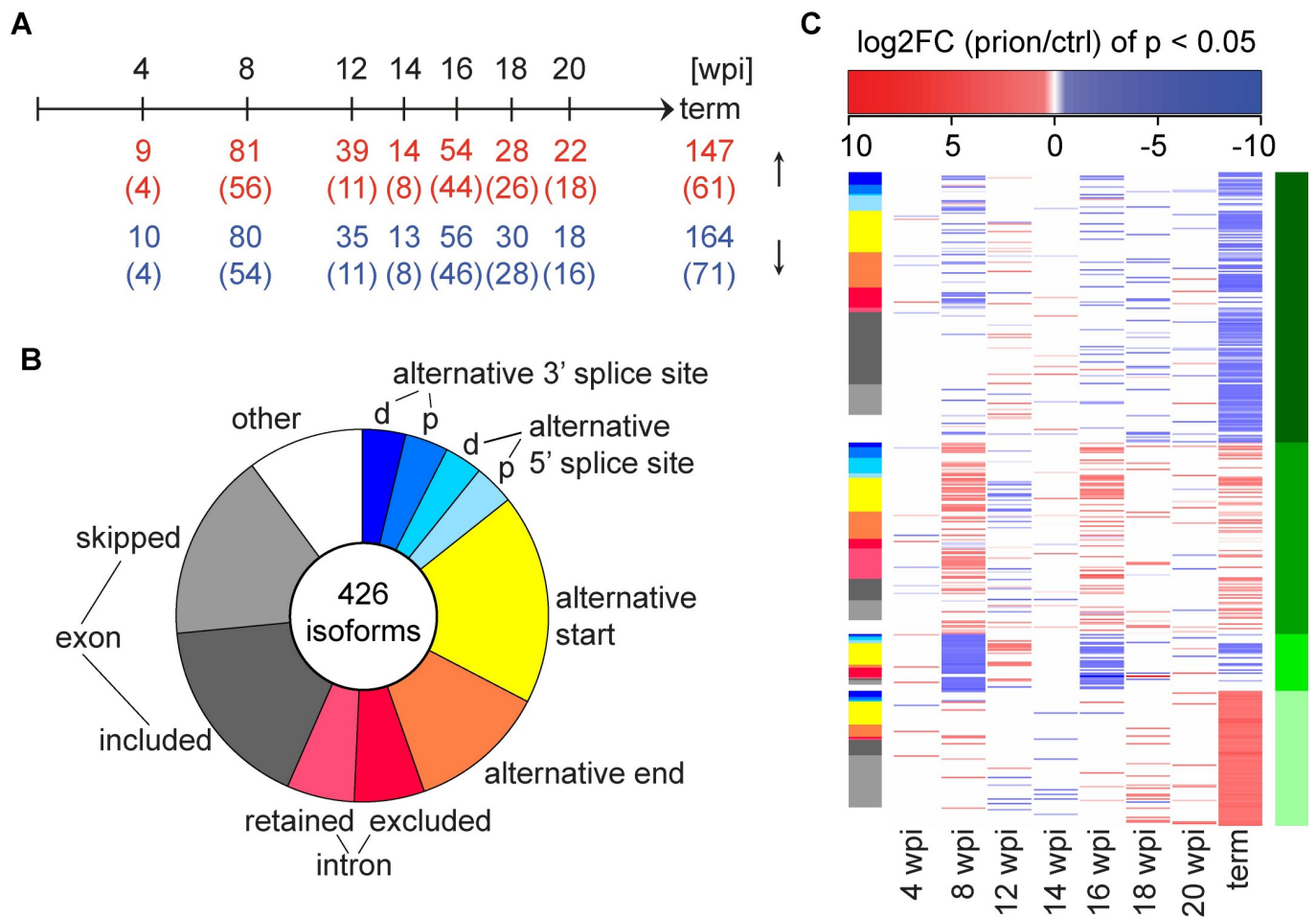


Fig 4. Post-transcriptional regulation during prion disease progression. **A** Time points of prion inoculations and differentially expressed splice isoforms (FDR < 0.05 at least at one time point). The number of upregulated and downregulated isoforms ($p < 0.05$) at each time point and the numbers of shared genes (in brackets) are indicated. **B** Pie chart representing splicing event percentages of 426 differentially expressed isoforms (FDR < 0.05 at least at one time point). d = distal, p = proximal. **C** Heat map depicting the \log_2FC of differentially expressed isoforms (only \log_2FC with $p < 0.05$ are colored). The corresponding splicing event (same coloring as in **B**) is indicated as a side bar on the left. Unsupervised kmeans clustering ($k = 4$ clusters) identified coherent patterns of \log_2FC . Clusters c1-4 are indicated as a side bar on the right.

<https://doi.org/10.1371/journal.ppat.1008653.g004>

event[21] increases both at 8 wpi as well as the terminal stage. Similarly, alternative splicing of the synapsin genes, *Syn1* and *Syn2*, and of *Ctsa*, a disease associated microglia (DAM) gene [22] changes at both 8wpi and the terminal stage. While mRNA levels of *Ctsa* increased at the terminal stage, they remained unchanged at 8 wpi, indicating that the regulation of splicing and mRNA abundance of this gene are unlinked.

A further post-transcriptional mechanism that is essential for nervous system homeostasis is RNA editing, whose dysregulation has been implicated in neurodegeneration[23]. The most common form of RNA editing, adenosine (A) to inosine (I) conversion, is mediated by the adenosine deaminase acting on RNA (ADAR). The expression levels of the ADAR enzymes, *Adar1* and *Adarb2* did not change during prion disease progression, whereas *Adarb1* was significantly downregulated at the terminal stage (S3 Table). Consistently, we did not observe major editing changes at any of the analyzed time points.

The impact of aging on prion disease progression

The prevalence of neurodegenerative diseases increases drastically with age. Sporadic CJD typically manifests in 55–65 years old individuals[24]. This age in humans is comparable to approximately 12 months of age in mice[25]. To assess if age-related changes accelerate prion disease progression, we compared disease progression in young vs. aged mice. We inoculated a third cohort of 2-month old “young” mice (similar to cohorts #1/2) and 1-year old mice. We analyzed gene expression changes at 8 wpi in aged mice and at the terminal stage in young and aged mice. Similar to the previously analyzed samples, we observed a separation of control and prion-inoculated samples at 8 wpi and the terminal stage (S5 Fig, S9 Fig and S9 Table). Remarkably, the median lifespan of aged prion-inoculated mice was only slightly, albeit significantly ($p = 0.0001$), shorter than that of young inoculated mice (Fig 5A). This suggests that age does not strongly accelerate prion disease progression and that disease manifestation is similar in young and aged mice. Consistently, a correlation of gene expression changes was noticeable at 8 wpi ($R = 0.39$; Fig 5B). Unsurprisingly, the changes in gene expression in young and aged mice converged towards the terminal stage ($R = 0.89$; Fig 5C).

Young plasma treatment ameliorates prion disease progression

Infusion of plasma from young mice can revert age-related impairments of cognition and synaptic plasticity[26] and ameliorates neuronal hippocampal dysfunctions in murine models of Alzheimer’s Disease[27]. We therefore analyzed the impact of young plasma on the course of prion disease as well as on the early prion-induced changes at 8wpi. Mice inoculated with prions or control brain homogenate were treated for 8 weeks with young plasma or saline via bi-weekly intravenous injections. Hippocampal samples were subjected to high-throughput sequencing at 8 wpi and at the terminal stage (S5 Fig, S10 Fig and S10 Table). We also monitored the rotarod performance and assessed mice for neurological signs from 18 wpi onwards by scoring for the absence/presence of a hunched posture, rigid tail, piloerection, hind limb clasp and ataxia (Fig 6A). Remarkably, plasma administration reduced essentially all prion-induced changes at 8 wpi (Fig 6B). Neurological deficits, which usually occur at 20 wpi, became evident only at 23 wpi in plasma-treated animals (Fig 6C). Similarly, rotarod performance decreased at a later stage in plasma-treated samples (S10 Fig). In contrast, we only observed a mild, non-significant increase in the median lifespan upon plasma administration (Fig 6D), and, as expected, the terminal prion-induced changes were very similar between plasma and saline-treated mice (Fig 6E). This suggests that young plasma treatment might improve the health span but not the lifespan of prion diseased mice.

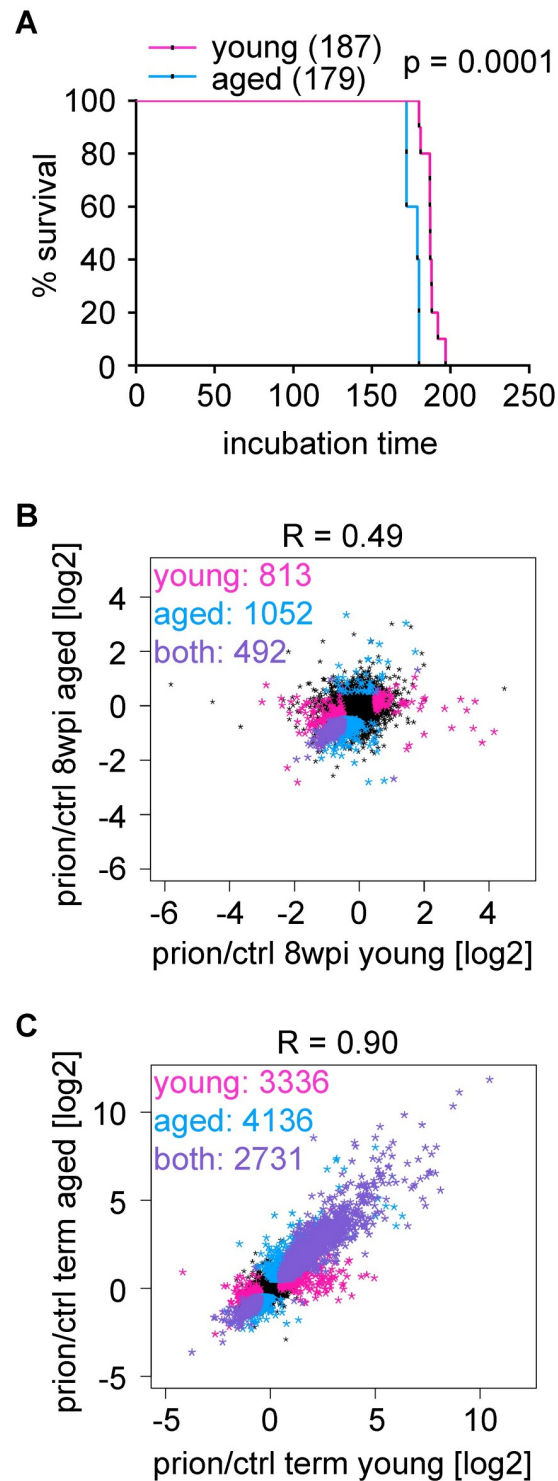


Fig 5. Impact of aging on prion disease progression. **A** Survival curves of mice inoculated at 2 months (young) or one year (aged). Shown is the % survival compared to days post inoculation (dpi). The median survival, which is significantly reduced in aged mice ($p = 0.0001$; log-rank Mantel-Cox test) is indicated. **B** Scatter plot comparing the \log_2 FC of expressed genes in young and aged prion-inoculated mice at 8 wpi. Genes that are differentially expressed ($|\log_2\text{FC}| > 0.5$ and $\text{FDR} < 0.05$) in young ($n = 813$) or aged ($n = 1,052$) mice are colored in pink and blue, respectively. The change in expression correlates ($R = 0.39$) and 492 genes change both in young and aged mice (colored in purple). **C** Scatter plot comparing the \log_2 FC of expressed genes in young and aged prion-inoculated mice at the terminal stage.

Genes that are differentially expressed ($|\log_2FC| > 0.5$ and $FDR < 0.05$) in young ($n = 3,336$) or aged ($n = 4,136$) mice are colored in pink and blue, respectively. The change in expression is highly correlated ($R = 0.89$) and 2,731 genes change both in young and aged mice (colored in purple).

<https://doi.org/10.1371/journal.ppat.1008653.g005>

Discussion

Here we have correlated the temporal sequence of transcriptional, and splicing events with neuropathological changes, prion infectivity, and clinical signs, and have generated a searchable genome-wide database of prion-induced changes during disease progression. As expected, the histological alterations (microgliosis and astrogliosis, spongiform changes and PrP^{Sc} deposition) and clinical signs were mirrored by pronounced gene expression changes at terminal disease. Surprisingly, onset and progression of motor dysfunctions correlated precisely with the onset of glial changes and occurred long before neuronal loss was detectable. This suggests that glial perturbation, rather than neuronal demise, could be the driver of prion disease progression. Moreover, we observed pronounced PrP-dependent gene expression changes at 8 wpi, when neither neuropathological changes, prion infectivity, nor clinical symptoms are detectable. These early gene expression changes might provide new starting points for the development of novel therapeutics and diagnostics.

We further detected the differential expression of 426 splicing isoforms. Most splicing differences occurred both at terminal disease and at the preclinical 8 wpi timepoint. More than 100 of these splicing isoforms mapped to genes that were also differentially expressed, indicating that splicing and expression of these genes is linked. Nine genes were differentially spliced at multiple sites, including *App*, *Chl1*, *Evl*, *Fus*, *Neo1*, *Olfm1*, *Picalm*, *Ppfia4* and *Sorbs1*. Several of these genes have been linked to neurodegeneration, suggesting that splicing dysregulation of these genes might be common to multiple neurodegenerative diseases. In contrast, we could not identify a significant difference in RNA editing, even at the terminal disease stage. These results were inconsistent with a recent study[13], identifying a prion-induced editing signature in mouse cortex, which could at least partially be confirmed in human autopsy brain. It remains to be seen if prion-induced editing changes differ between brain regions, or if the use of distinct murine prion disease models accounts for this discrepancy.

Our experiments also show that prion titers never reach a plateau but continue to rise until the terminal stage of disease. PrP dependent gene expression changes occur in parallel with initial prion replication, while amounts of infectious units progressively increases over disease incubation time. Earlier investigations[6–8] have hypothesized that scrapie neurotoxicity is only triggered when a “lethal” form of prion protein (denoted “PrP^L”) accumulates in late pathogenesis, in a second phase of the disease, and drives toxicity and clinical disease. Conversely, prion replication would initially occur without associated toxicity. However, no physical evidence of “PrP^L” has ever surfaced. In addition, the two-phase hypothesis rests on the quantification of prion infectivity and histological analyses fraught with analytical imprecision and poor sensitivity. The discovery of early, specific, robust and reproducible PrP-dependent disease-associated gene expression changes before the saturation of prion infectivity refutes the two-phase hypothesis and suggests that pathology starts as soon as prions enter the brain.

Surprisingly, our analysis indicates that early alterations can be initially overcome. The existence of compensatory mechanisms is suggested by the oscillating gene expression patterns that were observed. The early downregulation of cluster-4 genes was transient and underwent complete recovery. Another peculiar expression profile was observable for certain microglial markers which were monotonically upregulated from 16 wpi. This included phagocytosis-related genes (*Aif1*, *Dock2*, *Fgr*, *Fcgr1*, *Fcgr2b*, and *Fcgr3*) and disease-associated microglia (DAM) genes (*Itgax*, *Clec7a*, *Cxcl10* and *Lag3*)[28]. Remarkably, the upregulation of these

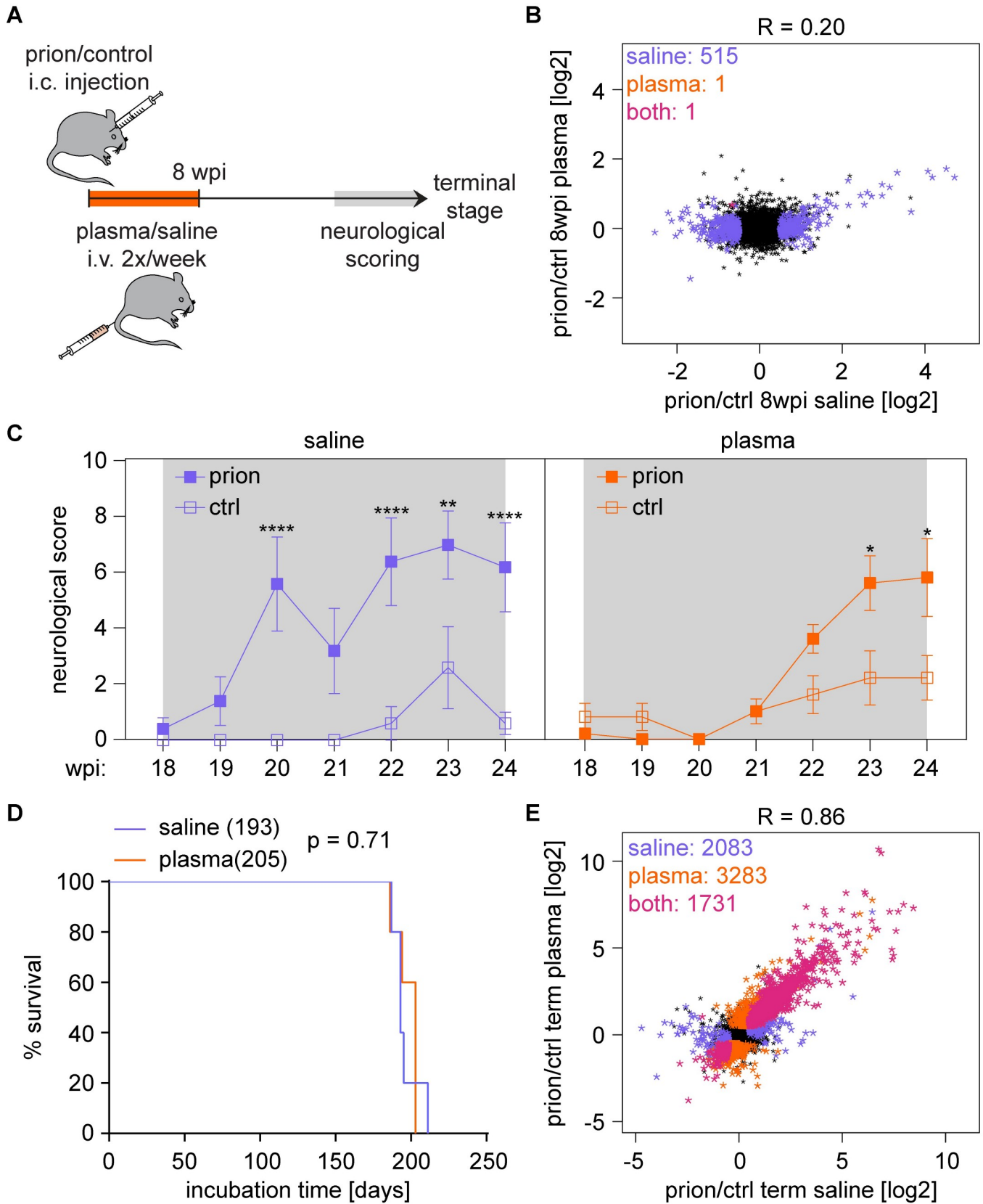


Fig 6. Young plasma treatment ameliorates prion disease progression. **A** Time points of prion inoculation, plasma treatment, neurological scoring and sample analysis. **B** Scatter plot comparing the \log_2FC of expressed genes in plasma and saline treated prion-inoculated mice at 8 wpi. Differentially expressed genes ($|\log_2FC| > 0.5$ and $FDR < 0.05$) are colored in purple (saline; $n = 515$) and orange (plasma; $n = 1$). **C** Plot displaying the neurological score of saline and plasma-treated mice from 18 wpi until the terminal stage. Shown is the mean neurological score \pm SEM (** $p < 0.01$; *** $p < 0.001$; **** $p < 0.0001$; two-way ANOVA followed by Tukey's multiple comparison test comparing prion vs control samples at each time point). **D** Survival curves of mice that were treated for 8 weeks with saline or plasma after prion inoculation. Shown is the % survival compared to days post inoculation (dpi). The median survival of plasma treated mice did not change ($p = 0.71$; log-rank Mantel-Cox test). **E** Scatter plot comparing the \log_2FC of expressed genes in plasma and saline treated prion-inoculated mice at the terminal stage. Differentially expressed genes ($|\log_2FC| > 0.5$ and $FDR < 0.05$) are colored in purple (saline; $n = 2,083$), orange (plasma; $n = 3,283$) or pink (both; $n = 1,730$).

<https://doi.org/10.1371/journal.ppat.1008653.g006>

genes correlates precisely with the onset of motor deficits whereas no such correlation existed with neuronal genes. We therefore hypothesize that it is glial rather than any neuronal alterations that cause clinical disease manifestation. This aligns with gliosis being observed in symptomatic but not in pre-symptomatic CJD patients[29]. Alternatively, the dysfunction of a small number of neurons at 16–18 wpi may drive clinical signs while remaining below the detection threshold of RNAseq.

Clinically overt Creutzfeldt-Jakob disease progresses much more quickly than most other neurodegenerative syndromes, making the development of effective therapies extremely difficult. However, our data suggest that the critical period for potential intervention may be much earlier than previously estimated[6,10]. Accordingly, infusion of young plasma during the first 8 weeks after prion inoculation attenuated the early downregulation of genes involved in neuronal functions, and also delayed the manifestation of neurological signs as observed in models of Alzheimer's disease[27]. Interestingly, the beneficial effects of young plasma did not translate into a significantly extended overall survival, perhaps because primary prion replication was not modified despite attenuated downstream neurotoxicity. Similarly, the survival curves of young and middle-aged prion inoculated mice were similar, suggesting that ageing has only minor effects on early and late transcriptional changes as well as lifespan. And yet the plasma experiment suggests that treatment aimed at rescuing the molecular alterations identified in the clinically silent phase might impact the consequent entire progression of the disease. This idea is also in line with emerging results of novel potential therapies which seem to be effective only when started either prophylactically or within the first 11 weeks after prion inoculation [30]. The fact that young plasma seems to improve the health span, rather than the lifespan, of prion disease may be relevant to improving the life quality of patients with neurodegenerative diseases.

It remains to be seen whether the molecular phenomena and kinetics detected in mouse models of prion disease reflect those of the corresponding human disorders. If so, the results detailed here may instruct the development of early diagnostic and therapeutic approaches. Finally, the molecular mechanisms underlying prion diseases may also be of relevance for other common protein misfolding disorders, such as Alzheimer's and Parkinson's disease.

Methods

Mice

Animal experiments were performed in compliance with the Swiss Animal Protection Law, under the approval of the Veterinary office of the Canton Zurich (animal permits ZH41/2012, ZH90/2013, ZH040/15, ZH243/15). All efforts were made to prevent or minimize animal discomfort and suffering; individual housing was avoided. Prion-inoculated and control-injected mice were regularly monitored for the development of clinical signs, according to well established procedures. Humane termination criteria were employed. Intracerebral injections, blood collection and transcardial perfusions were performed in deeply anesthetized mice. Habituation periods before experiment begin were included. Housing conditions and details

of animal experimentation are detailed in the corresponding sections. C57BL/6J male mice were purchased from Charles River, Germany. C57BL/6J coisogenic *Prnp*^{ZH3/ZH3} knockout mice[31] were bred in house. Mice were kept in a conventional hygienic grade facility, constantly monitored by a sentinel program aimed at screening the presence of all bacterial, parasitic, and viral pathogens listed in the Federation of European Laboratory Animal Associations (FELASA). Animal facility was considered positive for *Murines Norovirus* and *Helicobacter spp.* Animals were kept in IVC type II long cages with autoclaved dust-free Lignocel SELECT Premium Hygiene Einstreu (140-160g/cage) (Hersteller J. Rettenmaier & Söhne GmbH), autoclaved 20 x 21 cm paper tissues (Zellstoff), autoclaved hay and a carton refuge mouse hut as nesting material. Up to five mice were housed in the same cage. Individual housing was avoided. For the plasma treatment experiment, 20 male mice were kept in groups of 5 in individually ventilated type II cages in a highly hygienic grade facility. Mice had unrestricted access to sterilized drinking water and were fed a pelleted mouse diet (Kliba No. 3340 or 3341, Provimi Kliba, Kaiseraugst, Switzerland) *ad libitum*. The light/dark cycle consisted of 12/12 h with artificial light (40 Lux in the cage) from 07:00 to 19:00h. The temperature in the room was 21 ±1 °C, with a relative humidity of 50±5%. The air pressure was controlled at 50 Pa, with 15 complete changes of filtered air per hour (HEPA H 14 filter; Vokes-Air, Uster, Switzerland).

Prion inoculations

Imported mice were allowed at least one week of habituation in our animal facility before experimental manipulations. Six-week or 51-week old C57BL/6 male mice (S1 Table) were injected in the right hemisphere with 30 µl of RML6 (passage 6 of Rocky Mountain Laboratory strain mouse-adapted scrapie prions) at a 10⁻² dilution of a 10% homogenate, containing 9.02 log LD₅₀ of infectious units per ml in 10% homogenate. Control inoculations were performed using 30 µl of non-infectious brain homogenate (NBH) from CD-1 mice at the same dilution. Each experimental mouse was randomly assigned a code and, based on this, to an experimental group/time point. After inoculation, mice were initially monitored three times per week. After clinical onset, mice were daily monitored. Mice were sacrificed at pre-defined time points based on their experimental group, starting always at the same time of the day and alternating between prion-inoculated and NBH-injected mice. Prion-inoculated mice allocated to the terminal group were sacrificed upon clear signs of terminal prion disease. Control-injected mice assigned to the latest time point group were sacrificed at 192 days post-inoculation, 13 days later than the last terminal prion-inoculated mouse. Transcardial perfusion with ice-cold PBS was performed in deeply anesthetized mice.

For RNAsequencing, hippocampi from both hemispheres were dissected, snap frozen and stored at -80°C until processing (S1 Table). For histologic analysis (S6 Fig), 15 additional C57BL/6J male mice were inoculated with RML6, and groups of 3 mice were sacrificed at the indicated time points. Dissected brains were fixed in formalin. For the rotarod analysis shown in Fig 3, 8 additional C57BL/6J male mice were inoculated with RML6.

Plasma collection and administration, and neurological scoring

Plasma preparation and administration was performed as previously described[26], with minor modifications. Peripheral blood was collected from 150 young (6 weeks old) mice using retro-orbital bleeding in deeply anesthetized mice who were then immediately sacrificed by decapitation. Pooled mouse plasma was separated from blood collected with EDTA by centrifugation at 1,000g, followed by dialysis using 3.5-kDa D-tube dialyzers (EMD Millipore) in PBS to remove EDTA, aliquoting and storage at -80°C until use. Systemic administration of either plasma or saline as control was performed by injection of 100µl in the tail vein of mice

who had received an intra-cerebral injection with either RML6 prions or NBH. Treatment started the day after the intracerebral injection and was performed twice weekly for 8 weeks. Mice were sacrificed at 8 wpi or the terminal stage ($n = 5$ per each group) by transcardial perfusion with ice-cold PBS in deeply anesthetized mice. Hippocampi from both hemispheres were dissected, snap frozen and stored at -80°C until processing. RNA extraction and sequencing were performed in two separate rounds (S1 Table) but were pooled for analysis.

Neurological scoring was performed weekly from 18 wpi until 24 wpi by an observer who was blinded to experimental group allocation (RML or NBH-injected, plasma- or saline-treatment), and encompassed the assignment of scores from 0 (no abnormality) to 1-2-3 (for mild, moderate or severe abnormalities) in the following domains: hunched posture, piloerection, rigid tail, hind limbs claspings, ataxia.

Immunohistochemistry

Histological analyses were performed on 2- μm thick sections from formalin fixed, formic acid treated, paraffin embedded brain tissues, as previously described[32]. Sections were subjected to deparaffinization through graded alcohols, followed by heat-induced antigen retrieval performed in EDTA-based buffer CC1 (Ventana). Stainings were performed on a NEXES immunohistochemistry robot (Ventana instruments) with the following antibodies: Iba1 (1:1000, Wako); GFAP (1:13000, Dako); SAF84 (1:200, SPI bio). For the latter staining, incubation with protease 2 (Ventana) was performed before antibody incubation. Immunoreactivity was visualized using an IVIEW DAB Detection Kit (Ventana). Haematoxylin and eosin stainings were performed according to standard procedures. Slides were scanned with NanoZoomer and images were acquired using the NanoZoomer Digital Pathology System (NDPview, Hamamatsu Photonics). High magnification pictures were quantified with an in-house developed python script by counting the number of HRP pixels, which were defined as pixels for which the following condition in RGB colour space holds true: $R > G > B$.

Rotarod

The rotarod test was performed as previously described[32], with minor modifications. The rotarod apparatus (Ugo Basile) consisted of a rotating cylinder ($\varnothing 3$ cm) subdivided in five 57-mm wide lanes by dividers ($\varnothing 25$ cm). Each test consisted in habituation phase and an experimental phase. The habituation phase comprised three sessions of 1 min each, at a constant speed of 5 rotations per minute (rpm), with inter-sessions intervals of at least 15 min. The test phase, which started at least 15 min after the last habituation trial, comprised three sessions of maximum 5 min each, at a constant acceleration from 5 rpm to maximum of 40 rpm, with inter-sessions intervals of at least 15 min. Latency to fall was calculated as the time until either falling from the drum or clinging to the rod and passively rotating with occurred. Rotarod tests were performed at the same time of the day (between 2 pm and 4 pm).

Standard scrapie cell assay

CAD5 cells were grown with standard OFBS Medium (Opti-MEM containing 10% FBS, 1% streptomycin and penicillin, 1% Glutamax; Gibco) in a T150 cell culturing flask. One day prior to infection, 10,000 CAD5 and CAD5 KO cells lacking PrP^C expression were plated with 100 μL OFBS in 96-well cell culture plates (TPP) and incubated at 37°C with 5% CO_2 . On the following day, 100 μL of brain homogenate diluted in OFBS mixed with 0.01% brain homogenate from C57BL/6J-*Prnp*^{ZH3/ZH3} mice to provide a complex matrix was added to the cells for the infection. To establish a standard curve for infection, a 1:5 serial dilution of RML6 brain homogenate (20% w/v in 0.32M sucrose, 10 LD₅₀ units per mL) was used with a range from

1×10^{-3} to 6.4×10^{-8} . For each sample, three different dilutions were performed ranging from 1×10^{-3} to 1×10^{-5} . To control for residual inoculum, CAD5 KO cells were incubated with RML brain homogenate corresponding to the highest concentration of the standard (0.01%). CAD5 cells were incubated with (0.01%) non-infectious brain homogenate (10% w/v in 0.32M sucrose) to control for efficient proteinase K (PK) (Roche) digestion and to compute the background of the assay. Three days following infection, cells were split 1:8 into new 96 well plates containing fresh OFBS. After reaching confluence, two additional 1:8 splitting steps were performed, corresponding to days 7 and 10 post infection. On day 14 post infection, ELISPOT membranes (Millipore) were activated by adding filtered 50 μ L ethanol/well, washed twice with 160 μ L PBS and nearly 40,000 cells per well transferred onto the membrane and dried with a plate thermomixer (Eppendorf) at 50°C. After drying, plates were stored at 4°C until lysis and digestion. 50 μ L of 0.5 ug/mL PK in lysis buffer (50 mM Tris-HCl pH8, 150 mM NaCl, 0.5% w/v sodium deoxycholate, 0.5% w/v Triton-X-100) was added to each well and incubated for 90 minutes at 37°C. Following incubation, vacuum was applied to discard the contents and wells were washed twice with 160 μ L PBS. To stop digestion, 160 μ L of 2 mM PMSF (Sigma Aldrich) diluted in PBS was applied to the membrane and incubated at room temperature for 10 min. Tris guanidinium thiocyanate was prepared by diluting 3 M guanidinium thiocyanate in 10 mM Tris HCl pH8, and added subsequently with a total volume of 160 μ L/well and incubated for 10 min. Supernatant was discarded into 2M NaOH and membrane was washed seven times with each 160 μ L PBS and blocked 1 h with 160 μ L Superblock (Thermo Scientific) prepared in MilliQ. Remaining blocking solution was removed under vacuum and 50 μ L POM1 antibody was applied at a concentration of 1:5000 diluted in TBST (10 mM Tris HCl, pH 8, 150 mM NaCl, 0.1% (v/v) Tween 20) containing 1% (w/v) non-fat dry milk for 1 h. Supernatant was discarded and wells were subsequently washed seven times with TBST under vacuum. 50 μ L of anti-IgG1-AP (Southern Biotechnology Associates) was used with a 1:4500 dilution in TBST-1% (w/v) non-fat dry milk and incubated for 1 h. Discarding of the supernatant and washing was performed in the same way as for the POM1 antibody. 50 μ L of AP dye (Bio-rad) for the reaction was applied and incubated for 16 minutes. Membrane was washed twice with water, dried and stored at -20°C in dark. Membranes were quantified using ImageJ (open source) with optical density, to distinguish between spots (representing cells that contain PK-resistant PrP) and clear areas. Data derived from SSCA have also been used for a scaling analysis to estimate rates of replication *in vivo* (Meisl et al., submitted).

Real-time quaking induced conversion assay (RT-QuIC)

RT-QuIC assays of prion-infected mouse brain homogenates were performed as previously described[33]. Briefly, recombinant full-length hamster PrP (23–231) was expressed in Rosetta2 (DE3)pLysS *E.coli* competent cells and purified from inclusion bodies by affinity chromatography using Ni²⁺-nitrilotriacetic acid Superflow resin (QIAGEN). Recombinant hamster PrP (HaPrP) was used as monomeric substrate protein for the RT-QuIC conversion. Mouse brain homogenates (20% in 0.32M sucrose) were diluted 2000-fold and used as seeds for the RT-QuIC conversion. RT-QuIC reactions containing HaPrP substrate protein at a final concentration of 0.1 mg/ml in PBS (pH 7.4), 170 mM NaCl, 10 μ M EDTA, 10 μ M Thioflavin T were seeded with 2 μ L of diluted brain homogenates in a total reaction volume of 100 μ L. NBH- and RML6-treated brain homogenates were used as negative and positive controls, respectively. The RT-QuIC reactions were amplified at 42°C for 100 h with intermittent shaking cycles of 90 s shaking at 900 rpm in double orbital mode and 30 s resting using a FLUOstar Omega microplate reader (BMG Labtech). Aggregate formation was followed by measuring the thioflavin T fluorescence every 15 min (450 nm excitation, 480 nm emission; bottom read mode).

RNA, extraction, library preparation and sequencing

RNA was extracted from snap frozen brain areas (both hemispheres for hippocampus) using the RNeasy Plus Universal Kit (QIAGEN), following manufacturer's instructions. Quantity and quality of RNA were analyzed with Qubit 1.0 Fluorometer (Life Technologies) and Bioanalyzer 2100 (Agilent Technologies), respectively. The TruSeq RNA Sample Prep kit v2 (Illumina) was employed for library preparation. In brief, 1 μ g of total RNA per sample was poly A enriched, reverse transcribed into double-stranded cDNA and then ligated with TruSeq adapters. PCR was performed to selectively enrich for fragments containing TruSeq adapters at both termini. Quantity and quality of enriched libraries were analyzed using Qubit (1.0) Fluorometer and Caliper GX LabChip GX (Caliper Life Sciences). The resulting product is a smear with a mean fragment size of approximately 260 bp. Libraries were then normalized to 10 nM in Tris-Cl 10 mM, pH 8.5, with 0.1% (vol/vol) Tween 20. Cluster generation was performed with the TruSeq PE Cluster kit v4-cBot-HS (Illumina), using 2 pM of pooled normalized libraries on the cBOT. Sequencing was performed on Illumina HiSeq 4000 paired-end at 2×126 bp using the TruSeq SBS kit v4-HS (Illumina).

Data analysis

Alignment and feature counting. RNA sequencing data analysis was performed as previously described[34], with modifications. Quality control of reads was performed using FastQC. Low-quality ends were clipped (5': 3 bases; 3': 10 bases). Trimmed reads were aligned to the reference genome and transcriptome (FASTA and GTF files, respectively, downloaded from the UCSC mm10) with STAR version 2.3.0e_r291[35] with default settings.

Differential gene expression. Differentially expressed genes were identified based on $|\log_2FC| > 0$ and $FDR < 0.05$ using the R package *edgeR*[36] from Bioconductor (version 3.0). Only genes with at least 10 counts in at least 50% of the samples in one of the groups were considered in the analysis. Differentially expressed genes (DEGs) were defined as genes changing with $|\log_2FC| > 0.5$ and $FDR < 0.05$. \log_2FC with $p \geq 0.05$ were set to 0 for unsupervised kmeans clustering, t-distributed stochastic neighbor embedding (t-SNE) and the comparison with rotarod performance (Figs 1B, 1C and 3B–3D, and S2 Fig). RNA isolated from saline and plasma-treated mice was isolated, processed and sequenced in two independent runs (indicated in S10 Fig). All saline and plasma-treated mice were analyzed together. An additional covariate was added to the model in *edgeR* to account for the batch effect associated with the different runs. To assess if DEGs changed at multiple time points (Fig 2A and 2C and S2 Fig) we lowered the cut-off to $|\log_2FC| > 0.5$ and $p < 0.05$.

Alternative splicing. Analysis of splice variants was performed by using SGseq[37] and DEXseq[38] R packages as described previously[39] with some modifications. SGseq was first applied to identify splicing events (e.g. cassette alternative exon) related to two or more variants (e.g. isoforms with exon included or exon skipped). Exons and splice junctions were predicted from BAM files. Predictions for each sample were merged to obtain a common set of transcript features, and exons were partitioned into disjoint exon bins. A genome-wide splice graph was assembled based on splice junctions and exon bins, and splice events were identified from the graph. To determine differential splicing events, a single value for each variant was produced by either adding up the 5' and 3' counts, or, if these represented the same transcript features, by considering the unique value. These counts then constituted the initial input to DEXSeq, as described in the SGSeq manual. Briefly, instead of quantifying differential usage of exons across a single gene, we analyzed differential usage of variants across a single event. Such adaptation of DEXSeq is also reported in the DEXSeq vignette. Similar to the differential gene expression analysis, we retained only variants with at least five counts in at least three samples

(of any condition). After this filtering step, in events associated with a unique variant, such variant was considered to be constitutive and discarded. For most comparisons, these two filters reduced the total number of variants tested to around 6,000. Differential analysis was then performed implementing a sample+exon+condition: exon model in DEXSeq. To limit the number of tests, the first variant of each event (generally a 'skipping' variant) was discarded. As our data, possibly due to the Nugen amplification, shows high levels of intronic reads, retained intron events were also discarded. Differentially expressed isoforms were defined as isoforms changing with $FDR < 0.05$. \log_2FC with $p \geq 0.05$ were set to 0 for unsupervised kmeans clustering (Fig 4C). To compare if splicing isoforms were differentially expressed at multiple time points (Fig 4A) we lowered the cut-off to $p < 0.05$.

RNA editing. A list of putative RNA-editing sites was compiled by intersecting the results of REDIttools[40] and VarScan2[41]. In particular, we required the following six criteria to be fulfilled in both workflows: 1) a minimum mapping quality of 20 and a minimum base quality of 25; 2) a minimum total coverage of 10 reads and a minimum non-reference allele coverage of 3; 3) a p-value threshold of 0.05 in both REDIttools and VarScan2 tests; 4) a minimum editing frequency of 1%; 5) an A-to-G or T-to-C nucleotide exchange; and 6) the editing site did not correspond to a dbSNP variant. The resulting vcf file contained ~26,000 putative RNA editing sites and was annotated using SnpEff v4.3[42]. For pair-wise comparisons between groups, only sites with reads supporting an editing event in two out three samples per group were reported. P values were calculated using a two-tailed t test and Benjamini-Hochberg adjusted for multiple testing.

Database comparisons. As previously described[31] a list of genes enriched in neurons, astrocytes, oligodendrocytes, microglia and CNS endothelial cells (500 genes per cell type) was retrieved using the cell type enrichment query from a transcriptomic based database, (http://web.stanford.edu/group/barres_lab/brain_rnaseq.html)[16], searching for genes enriched in one cell type respect to all others. In the case of oligodendrocytes, myelinating oligodendrocytes, newly formed oligodendrocytes and oligodendrocytes precursor cells were considered together. The resulting, non-overlapping list of CNS cell-type enriched genes was used for comparisons with the lists of genes with differential gene expression, and alternative splicing in the present study.

Gene Ontology analyses were performed with GORILLA (<http://cbl-gorilla.cs.technion.ac.il>), comparing indicated gene lists with a list of expressed genes.

Data visualization. Data was visualized in R using the packages DESeq2, RColorBrewer, pheatmap, gplots, ggplot2, NbClust, factoextra, eulerr, tidyverse, datasets, data.table, and circlize. Center lines of boxplots show the median, vertical boxes represent the inter-quartile range (IQR) and whiskers represent $1.5 \times IQR$. Data points beyond that distance are plotted as single points. t-distributed Stochastic Neighbor Embedding (t-SNE) method was used for projecting high dimensional gene expression data in a 2D space. We used the t-SNE implementation from scikit-learn library in Python with the following parameters: learning rate = 200, n iter = 1,000, random state = 0, metric = Euclidean, init = pca.

Code availability

Code is available from the authors by request.

Supporting information

S1 Fig. Sample separation during prion disease progression. **a**, Hierarchical clustering based on Euclidean distances. Heatmaps depicting the sample distances at each time point based on RNAseq expression data. Control and prion-injected samples cluster from 18 wpi onwards. **b**,

Principal component analysis of RNAseq samples at different time points revealing a separation of control (green) and prion-injected (blue) samples at 8 wpi, 20 wpi and the terminal stage.

(TIF)

S2 Fig. Distribution of cell-type enriched genes among DEGs. **a**, Table displaying the number of genes enriched in the different cell types and which cluster they belong to. **b**, Heat maps depicting the \log_2FC of DEGs known to be enriched in different cell types (only \log_2FC with $p < 0.05$ are colored). The corresponding clusters are indicated as a side bar. The height of the heatmap corresponds to the number of genes. **c**, Schematic depicting time points of prion inoculations. Number of upregulated and downregulated DEGs ($|\log_2FC| > 0.5$ and $p < 0.05$), and numbers of shared genes (in brackets) are indicated. **d-f**, Percentages of cell-type enriched genes within upregulated mDEGs (c), downregulated mDEGs (d) and downregulated genes at different time points (e).

(TIF)

S3 Fig. Validation of mRNA expression changes in a second, validation cohort. **a**, Hierarchical clustering based on Euclidean distances. Heatmaps depicting the sample distances based on RNAseq expression data. Control and prion-injected samples cluster at 8 wpi, and the terminal stage. **b**, Principal component analysis of RNAseq samples revealing a separation of control (green) and prion-injected (blue) samples at 8 wpi, and the terminal stage. **c**, Scatter plot depicting expressed genes. The change in expression at 8 wpi correlates between the main and the validation datasets ($R = 0.29$). Genes belonging to the clusters identified in Fig 1 are colored. **d**, Boxplots representing the \log_2FC distribution in the main (left panel) and validation (right panel) datasets at 8 wpi. Only expressed genes are included. The distribution of all genes (black) and genes belonging to the clusters identified in Fig 1 are shown. The difference in the \log_2FC distribution between expressed genes and cluster 4 genes was assessed with a t test. **e**, Scatter plot depicting expressed genes. The change in expression at the terminal stage highly correlates ($R = 0.80$) and genes belonging to the clusters identified in Fig 1 are colored. **f**, Boxplots representing the \log_2FC distribution in the main (left panel) and validation (right panel) datasets at the terminal stage. Only expressed genes are included. The distribution of all genes (black) and genes belonging to the clusters identified in Fig 1 are shown. The difference in the \log_2FC distribution between expressed genes and cluster 4 genes was assessed with a t test.

(TIF)

S4 Fig. Validation of mRNA expression changes in PrP knockout mice and intraperitoneally inoculated mice. **a**, Hierarchical clustering based on Euclidean distances. Heatmaps depicting the sample distances based on RNAseq expression data. Control and prion-injected samples cluster at the terminal stage in intraperitoneally (i.p.) inoculated wild-type mice but not in intracerebrally (i.c.) inoculated PrP knockout (KO) mice, nor in intraperitoneally inoculated wild-type mice at 8 wpi. **b**, Principal component analysis of RNAseq samples revealing a separation of control (green) and prion-injected (blue) samples of intraperitoneally inoculated wild-type mice at the terminal stage. **c**, Boxplots representing the \log_2FC distribution of intracerebrally inoculated PrP knockout mice at 8 wpi and of intraperitoneally inoculated wild-type mice at 8 wpi and the terminal stage. Only expressed genes are included. The distribution of all genes (black) and genes belonging to the clusters identified in Fig 1 are shown. The difference in the \log_2FC distribution between expressed genes and cluster 4 genes was assessed with a t test.

(TIF)

S5 Fig. Cross-correlation plots comparing all 8 wpi and terminal samples. **a**, Cross-correlation plot of all 8 wpi comparisons included in this manuscript (main, validation, PrP knockout

(ko), intraperitoneally (ip) inoculated, aged, saline-treated, plasma-treated). Shown are scatter plots comparing the 8 wpi \log_2 FC between the groups and the corresponding R values (scaled according to R value). The PrP knockout samples do not correlate with any other sample. Among the others, the plasma-treated sample correlates least with the other 8 wpi samples. Only expressed genes are included. **b**, Cross-correlation plot of all terminal comparisons included in this manuscript (main, validation, intraperitoneally (ip) inoculated, young, aged, saline-treated, plasma-treated). Shown are scatter plots comparing the terminal \log_2 FC between the groups and the corresponding R values (scaled according to R value). All samples strongly correlate with each other. Only expressed genes are included. (TIF)

S6 Fig. Characterization of neuropathological changes. **a**, Survival curve of mice sacrificed at the terminal stage. Shown is % survival compared to days post inoculation (dpi). **b**, Quantification of high magnification images (including representative images shown in **d**). Error bars indicate standard deviations. **c**, Prion-inoculated mice were sacrificed at the indicated time points during disease progression. Brain sections were stained with hematoxylin and eosin (H&E), GFAP (astrocyte marker), IBA1 (microglia marker) and SAF84 (detects only PrP^{Sc} after protease treatment). Shown are representative pictures at each timepoint. Rectangles correspond to approximate location of higher-magnification images shown in **d**. Scale bar in upper left panel: 250 μ m (applicable to all panels). **d**, Higher-magnification images of GFAP, IBA1 and SAF84 stainings shown in **c**. Scale bar in upper left panel: 100 μ m (applicable to all panels). (TIF)

S7 Fig. Assessment of prion infectivity. **a**, RT-QuIC reactions using brain homogenates of mice inoculated with prions and sacrificed at indicated time points. Each sample was tested in quadruplicates, and each plot corresponds to one mouse ($n = 6$). RFU: relative fluorescence units. **b**, Dot plot graph showing infectious units measured by standard scrapie cell assay (SSCA). Each dot represents one mouse, bars indicate standard deviations. 6 (out of 6) samples at 4wpi and 3 (out of 6) samples at 8 wpi were below the limit of detection (LOD). P values were calculated with a one-way ANOVA followed by Tukey's multiple comparison test (** $p < 0.001$; compared to terminal). (TIF)

S8 Fig. Differentially spliced isoforms during prion disease progression. (Alternative) exons are shown in grey. Exons and introns are not drawn to scale. Average per-base exon read coverage and junction counts normalized to total read counts in control and prion diseased mice at the terminal time point are shown. Splicing events in *Picalm* (a), *App* (b), *Syn1* (c), *Syn2* (d), and *Ctsa* (e) were visualized with the plotSpliceGraph function of the SGSeq package in R. Shown events are indicated in [S8 Fig](#). (TIF)

S9 Fig. Impact of aging on prion disease progression. **a**, Hierarchical clustering based on Euclidean distances. Heatmaps depicting the sample distances based on RNAseq expression data. Control and prion-injected samples cluster at 8 wpi and the terminal stage in aged mice, and at the terminal stage in young mice. **b**, Principal component analysis of RNAseq samples revealing a separation of control (green) and prion-injected (blue) samples at 8 wpi and the terminal stage in aged mice, and at the terminal stage in young mice. (TIF)

S10 Fig. Young plasma treatment ameliorates prion disease progression. **a**, Hierarchical clustering based on Euclidean distances. Heatmaps depicting the sample distances based on

RNAseq expression data. Samples cluster predominantly according to cohorts. **b**, Principal component analysis of RNAseq samples revealing a separation of control (green) and prion-injected (blue) samples at the terminal stage. Samples additionally separated according to the run of RNA isolation/processing/sequencing (run #1 versus run #2). The batch effect of the different run was accounted for during the analysis. **c**, Rotarod performance of saline (left panel) and plasma-treated (right panel) prion-inoculated mice at specified time points during disease progression (pre = pre-inoculation). Bar plots display the mean latency +/- SEM to fall in 100 seconds, with each dot representing one individual mouse. P values were calculated with a one-way ANOVA followed by Tukey's multiple comparison test (* $p < 0.05$; ** $p < 0.01$; *** $p < 0.001$; **** $p < 0.0001$; compared to 1 wpi). (TIF)

S1 Table. Summary table of 114 sequenced mice. Table including sequencing and sample ID, dataset, treatment, gender, and timepoints of injection and sacrifice. (XLSX)

S2 Table. Expressed genes and all comparisons. Table containing GeneID, cell type enrichment if applicable (_NE = not enriched; AS = astrocytes; EC = endothelial cells; MG = microglia; N = neurons; OL = oligodendrocytes), Cluster (corresponding to clusters shown in Fig 1) and information on all edgeR comparisons of this manuscript. For each comparison expression, \log_2FC , P value and FDR are included. (TXT)

S3 Table. Prion-induced gene expression changes. Table containing 3,723 genes that are changing significantly ($|\log_2FC| > 0.5$ and $FDR < 0.05$) in at least one of the eight timepoints of the main dataset (Fig 1). Shown are GeneID, cell type enrichment if applicable (_NE = not enriched; AS = astrocytes; EC = endothelial cells; MG = microglia; N = neurons; OL = oligodendrocytes), cluster number (corresponding to clusters shown in Fig 1) and all eight edgeR comparisons related to the main dataset. For each comparison expression, \log_2FC , P value and FDR are included. (TXT)

S4 Table. GO analysis of mDEGs upregulated 16wpi. Gene Ontology analysis of terms related to biological processes, molecular function and cellular localization. 87 genes (85 of which were in the database) were upregulated from 16wpi onwards and were assessed for GO term enrichment compared to 16,127 expressed genes (15,493 of which were in the database). (XLSX)

S5 Table. GO analysis of mDEGs upregulated 18 wpi. Gene Ontology analysis of terms related to biological processes, molecular function and cellular localization. 440 genes (435 of which were in the database) were upregulated from 18 wpi onwards and were assessed for GO term enrichment compared to 16,127 expressed genes (15,493 of which were in the database). (XLSX)

S6 Table. GO analysis of terminally downregulated DEGs. Gene Ontology analysis of terms related to biological processes, molecular function and cellular localization. 1,081 genes (1,061 of which were in the database) were downregulated at the terminal stage and were assessed for GO term enrichment compared to 16,127 expressed genes (15,493 of which were in the database). (XLSX)

S7 Table. GO analysis of DEGs downregulated at 8 wpi. Gene Ontology analysis of terms related to biological processes, molecular function and cellular localization. 813 genes (800 of

which were in the database) were downregulated at 8 wpi and were assessed for GO term enrichment compared to 16,127 expressed genes (15,493 of which were in the database). (XLSX)

S8 Table. Differentially expressed splice isoforms. Table containing 426 splice isoforms that are differentially expressed ($FDR < 0.05$) in at least one of the eight timepoints of the main dataset (Fig 4). Shown are merged, group and feature ID, genomic coordinates (chromosome, start, end, width, strand), the corresponding transcript, variant type, cell type enrichment if applicable ($_NE$ = not enriched; AS = astrocytes; EC = endothelial cells; MG = microglia; N = neurons; OL = oligodendrocytes), cluster number (corresponding to clusters shown in Fig 4), and information on all eight DEXSeq comparisons on the main dataset. For each comparison isoform expression of ctrl and prion samples, \log_2FC , P value and FDR are included, and which isoforms are shown in S8 Fig is indicated. 102 splice isoforms map to genes that are differentially expressed in the main dataset. The respective RNA expression information is included for these 102 entries: cluster number (corresponding to clusters shown in Fig 1), and all eight edgeR comparisons related to the main dataset (expression, \log_2FC , P value and FDR). (XLSX)

S9 Table. Aging-related gene expression changes. Table containing 5,613 genes that are changing significantly ($|\log_2FC| > 0.5$ and $FDR < 0.05$) in at least one of the four comparisons related to the aging dataset (8wpi_main, 8wpi_old, term_young, term_old). Shown are GeneID, cell type enrichment if applicable ($_NE$ = not enriched; AS = astrocytes; EC = endothelial cells; MG = microglia; N = neurons; OL = oligodendrocytes), cluster number (corresponding to clusters shown in Fig 1), and information on the four edgeR comparisons related to the aging dataset. For each comparison expression, \log_2FC , P value and FDR are included. (TXT)

S10 Table. Plasma-induced gene expression changes. Table containing 3,956 genes that are changing significantly ($|\log_2FC| > 0.5$ and $FDR < 0.05$) in at least one of the four plasma dataset comparisons (8wpi_saline, 8wpi_plasma, term_saline, term_plasma). Shown are GeneID, cell type enrichment if applicable ($_NE$ = not enriched; AS = astrocytes; EC = endothelial cells; MG = microglia; N = neurons; OL = oligodendrocytes), cluster number (corresponding to clusters shown in Fig 1), and information on the four edgeR comparisons related to the plasma dataset. For each comparison expression, \log_2FC , P value and FDR are included. (TXT)

Acknowledgments

The authors acknowledge Catherine Aquino Fournier for RNA sequencing; Olga Romashkina, Ahmet Varol, Laura Cervantes, Karina Arroyo, Marianne König, Irina Abakumova, Rita Moos for excellent technical help; Magdalini Polymenidou, Marc Emmenegger, Alessandro Crimi, Assunta Senatore, Mark D. Robinson, Constance Ciaudo, Daniel Spies for discussion on data analyses, and members of the Aguzzi laboratory for critical comments, Tony Wyss-Coray and Joseph M. Castellano for sharing their protocol for young-plasma treatment and for discussions, and Simon Stephan, Norbert Wey and André Wethmar for building the searchable database.

Author Contributions

Conceptualization: Silvia Sorce, Mario Nuvolone, Claudia Scheckel, Adriano Aguzzi.

Data curation: Silvia Sorce, Mario Nuvolone, Daniel Heinzer, Merve Avar, Manuela Pfammatter, Petra Schwarz, Mirzet Delic.

Formal analysis: Giancarlo Russo, Andra Chincisan, Micha Müller, Despina Sanoudou, Claudia Scheckel.

Funding acquisition: Adriano Aguzzi.

Supervision: Simone Hornemann, Adriano Aguzzi.

Writing – original draft: Silvia Sorce, Mario Nuvolone, Giancarlo Russo, Adriano Aguzzi.

Writing – review & editing: Silvia Sorce, Mario Nuvolone, Giancarlo Russo, Claudia Scheckel, Adriano Aguzzi.

References

1. Aguzzi A, Calella AM. Prions: protein aggregation and infectious diseases. *Physiol Rev*. 2009; 89: 1105–1152. <https://doi.org/10.1152/physrev.00006.2009> PMID: 19789378
2. Swerdlow AJ, Higgins CD, Adlard P, Jones ME, Preece MA. Creutzfeldt-Jakob disease in United Kingdom patients treated with human pituitary growth hormone. *Neurology*. 2003; 61: 783–791. <https://doi.org/10.1212/01.wnl.0000084000.27403.15> PMID: 14504321
3. Collinge J, Whitfield J, McKintosh E, Beck J, Mead S, Thomas DJ, et al. Kuru in the 21st century—an acquired human prion disease with very long incubation periods. *Lancet Lond Engl*. 2006; 367: 2068–2074. [https://doi.org/10.1016/S0140-6736\(06\)68930-7](https://doi.org/10.1016/S0140-6736(06)68930-7)
4. Prusiner SB. Biology and genetics of prions causing neurodegeneration. *Annu Rev Genet*. 2013; 47: 601–623. <https://doi.org/10.1146/annurev-genet-110711-155524> PMID: 24274755
5. Aguzzi A, Nuvolone M, Zhu C. The immunobiology of prion diseases. *Nat Rev Immunol*. 2013; 13: 888–902. <https://doi.org/10.1038/nri3553> PMID: 24189576
6. Collinge J. Mammalian prions and their wider relevance in neurodegenerative diseases. *Nature*. 2016; 539: 217–226. <https://doi.org/10.1038/nature20415> PMID: 27830781
7. Sandberg MK, Al-Doujaily H, Sharps B, Clarke AR, Collinge J. Prion propagation and toxicity in vivo occur in two distinct mechanistic phases. *Nature*. 2011; 470: 540–542. <https://doi.org/10.1038/nature09768> PMID: 21350487
8. Sandberg MK, Al-Doujaily H, Sharps B, De Oliveira MW, Schmidt C, Richard-Londt A, et al. Prion neuropathology follows the accumulation of alternate prion protein isoforms after infective titre has peaked. *Nat Commun*. 2014; 5: 4347. <https://doi.org/10.1038/ncomms5347> PMID: 25005024
9. Hwang D, Lee IY, Yoo H, Gehlenborg N, Cho J-H, Petritis B, et al. A systems approach to prion disease. *Mol Syst Biol*. 2009; 5: 252. <https://doi.org/10.1038/msb.2009.10> PMID: 19308092
10. Majer A, Medina SJ, Niu Y, Abrenica B, Manguiat KJ, Frost KL, et al. Early mechanisms of pathobiology are revealed by transcriptional temporal dynamics in hippocampal CA1 neurons of prion infected mice. *PLoS Pathog*. 2012; 8: e1003002. <https://doi.org/10.1371/journal.ppat.1003002> PMID: 23144617
11. Xiang W, Windl O, Wunsch G, Dugas M, Kohlmann A, Dierkes N, et al. Identification of differentially expressed genes in scrapie-infected mouse brains by using global gene expression technology. *J Virol*. 2004; 78: 11051–11060. <https://doi.org/10.1128/JVI.78.20.11051-11060.2004> PMID: 15452225
12. Majer A, Medina SJ, Sorensen D, Martin MJ, Frost KL, Phillipson C, et al. The cell type resolved mouse transcriptome in neuron-enriched brain tissues from the hippocampus and cerebellum during prion disease. *Sci Rep*. 2019; 9: 1099. <https://doi.org/10.1038/s41598-018-37715-z> PMID: 30705335
13. Kanata E, Llorens F, Dafou D, Dimitriadis A, Thüne K, Xanthopoulos K, et al. RNA editing alterations define manifestation of prion diseases. *Proc Natl Acad Sci U S A*. 2019; 116: 19727–19735. <https://doi.org/10.1073/pnas.1803521116> PMID: 31492812
14. Aguzzi A, Lakkaraju AKK, Frontzek K. Toward Therapy of Human Prion Diseases. *Annu Rev Pharmacol Toxicol*. 2018; 58: 331–351. <https://doi.org/10.1146/annurev-pharmtox-010617-052745> PMID: 28961066
15. Moreno JA, Radford H, Peretti D, Steinert JR, Verity N, Martin MG, et al. Sustained translational repression by eIF2 α -P mediates prion neurodegeneration. *Nature*. 2012; 485: 507–511. <https://doi.org/10.1038/nature11058> PMID: 22622579

16. Zhang Y, Chen K, Sloan SA, Bennett ML, Scholze AR, O’Keeffe S, et al. An RNA-Sequencing Transcriptome and Splicing Database of Glia, Neurons, and Vascular Cells of the Cerebral Cortex. *J Neurosci*. 2014; 34: 11929–11947. <https://doi.org/10.1523/JNEUROSCI.1860-14.2014> PMID: 25186741
17. Anthony K, Gallo J-M. Aberrant RNA processing events in neurological disorders. *Brain Res*. 2010; 1338: 67–77. <https://doi.org/10.1016/j.brainres.2010.03.008> PMID: 20226177
18. Harold D, Abraham R, Hollingworth P, Sims R, Gerrish A, Hamshere ML, et al. Genome-wide association study identifies variants at CLU and PICALM associated with Alzheimer’s disease. *Nat Genet*. 2009; 41: 1088–1093. <https://doi.org/10.1038/ng.440> PMID: 19734902
19. Klebig ML, Wall MD, Potter MD, Rowe EL, Carpenter DA, Rinchik EM. Mutations in the clathrin-assembly gene Picalm are responsible for the hematopoietic and iron metabolism abnormalities in fit1 mice. *Proc Natl Acad Sci U S A*. 2003; 100: 8360–8365. <https://doi.org/10.1073/pnas.1432634100> PMID: 12832620
20. Yao PJ, Petralia RS, Bushlin I, Wang Y, Furukawa K. Synaptic distribution of the endocytic accessory proteins AP180 and CALM. *J Comp Neurol*. 2005; 481: 58–69. <https://doi.org/10.1002/cne.20362> PMID: 15558718
21. Yamada T, Goto I, Sakaki Y. Neuron-specific splicing of the Alzheimer amyloid precursor protein gene in a mini-gene system. *Biochem Biophys Res Commun*. 1993; 195: 442–448. <https://doi.org/10.1006/bbrc.1993.2063> PMID: 8363619
22. Keren-Shaul H, Spinrad A, Weiner A, Matcovitch-Natan O, Dvir-Szternfeld R, Ulland TK, et al. A Unique Microglia Type Associated with Restricting Development of Alzheimer’s Disease. *Cell*. 2017; 169: 1276–1290.e17. <https://doi.org/10.1016/j.cell.2017.05.018> PMID: 28602351
23. Singh M. Dysregulated A to I RNA editing and non-coding RNAs in neurodegeneration. *Front Genet*. 2012; 3: 326. <https://doi.org/10.3389/fgene.2012.00326> PMID: 23346095
24. Aguzzi A. Prion diseases of humans and farm animals: epidemiology, genetics, and pathogenesis. *J Neurochem*. 2006; 97: 1726–1739. <https://doi.org/10.1111/j.1471-4159.2006.03909.x> PMID: 16805779
25. Dutta S, Sengupta P. Men and mice: Relating their ages. *Life Sci*. 2016; 152: 244–248. <https://doi.org/10.1016/j.lfs.2015.10.025> PMID: 26596563
26. Villeda SA, Plambeck KE, Middeldorp J, Castellano JM, Mosher KI, Luo J, et al. Young blood reverses age-related impairments in cognitive function and synaptic plasticity in mice. *Nat Med*. 2014; 20: 659–663. <https://doi.org/10.1038/nm.3569> PMID: 24793238
27. Middeldorp J, Lehallier B, Villeda SA, Miedema SSM, Evans E, Czirr E, et al. Preclinical Assessment of Young Blood Plasma for Alzheimer Disease. *JAMA Neurol*. 2016; 73: 1325–1333. <https://doi.org/10.1001/jamaneurol.2016.3185> PMID: 27598869
28. Keren-Shaul H, Spinrad A, Weiner A, Matcovitch-Natan O, Dvir-Szternfeld R, Ulland TK, et al. A Unique Microglia Type Associated with Restricting Development of Alzheimer’s Disease. *Cell*. 2017; 169: 1276–1290.e17. <https://doi.org/10.1016/j.cell.2017.05.018> PMID: 28602351
29. Iaccarino L, Moresco RM, Presotto L, Bugiani O, Iannaccone S, Giaccone G, et al. An In Vivo 11C-(R)-PK11195 PET and In Vitro Pathology Study of Microglia Activation in Creutzfeldt-Jakob Disease. *Mol Neurobiol*. 2018; 55: 2856–2868. <https://doi.org/10.1007/s12035-017-0522-6> PMID: 28455699
30. Minikel EV, Zhao HT, Le J, O’Moore J, Pitstick R, Graffam S, et al. Prion protein lowering is a disease-modifying therapy across prion strains, disease stages, and endpoints. *Neuroscience*; 2020 Mar. <https://doi.org/10.1101/2020.03.27.011940>
31. Nuvolone M, Hermann M, Sorce S, Russo G, Tiberi C, Schwarz P, et al. Strictly co-isogenic C57BL/6J-Prnp^{-/-} mice: A rigorous resource for prion science. *J Exp Med*. 2016; 213: 313–327. <https://doi.org/10.1084/jem.20151610> PMID: 26926995
32. Sorce S, Nuvolone M, Keller A, Falsig J, Varol A, Schwarz P, et al. The role of the NADPH oxidase NOX2 in prion pathogenesis. *PLoS Pathog*. 2014; 10: e1004531. <https://doi.org/10.1371/journal.ppat.1004531> PMID: 25502554
33. Pfammatter M, Andreasen M, Meisl G, Taylor CG, Adamcik J, Bolisetty S, et al. Absolute Quantification of Amyloid Propagons by Digital Microfluidics. *Anal Chem*. 2017; 89: 12306–12313. <https://doi.org/10.1021/acs.analchem.7b03279> PMID: 28972786
34. Nuvolone M, Kana V, Hutter G, Sakata D, Mortin-Toth SM, Russo G, et al. SIRPα polymorphisms, but not the prion protein, control phagocytosis of apoptotic cells. *J Exp Med*. 2013; 210: 2539–2552. <https://doi.org/10.1084/jem.20131274> PMID: 24145514
35. Dobin A, Davis CA, Schlesinger F, Drenkow J, Zaleski C, Jha S, et al. STAR: ultrafast universal RNA-seq aligner. *Bioinforma Oxf Engl*. 2013; 29: 15–21. <https://doi.org/10.1093/bioinformatics/bts635> PMID: 23104886

36. Robinson MD, McCarthy DJ, Smyth GK. edgeR: a Bioconductor package for differential expression analysis of digital gene expression data. *Bioinforma Oxf Engl.* 2010; 26: 139–140. <https://doi.org/10.1093/bioinformatics/btp616> PMID: 19910308
37. Goldstein LD, Cao Y, Pau G, Lawrence M, Wu TD, Seshagiri S, et al. Prediction and Quantification of Splice Events from RNA-Seq Data. *PLoS One.* 2016; 11: e0156132. <https://doi.org/10.1371/journal.pone.0156132> PMID: 27218464
38. Anders S, Reyes A, Huber W. Detecting differential usage of exons from RNA-seq data. *Genome Res.* 2012; 22: 2008–2017. <https://doi.org/10.1101/gr.133744.111> PMID: 22722343
39. Srinivasan K, Friedman BA, Larson JL, Lauffer BE, Goldstein LD, Appling LL, et al. Untangling the brain's neuroinflammatory and neurodegenerative transcriptional responses. *Nat Commun.* 2016; 7: 11295. <https://doi.org/10.1038/ncomms11295> PMID: 27097852
40. Picardi E, Pesole G. REDIttools: high-throughput RNA editing detection made easy. *Bioinforma Oxf Engl.* 2013; 29: 1813–1814. <https://doi.org/10.1093/bioinformatics/btt287> PMID: 23742983
41. Koboldt DC, Zhang Q, Larson DE, Shen D, McLellan MD, Lin L, et al. VarScan 2: somatic mutation and copy number alteration discovery in cancer by exome sequencing. *Genome Res.* 2012; 22: 568–576. <https://doi.org/10.1101/gr.129684.111> PMID: 22300766
42. Cingolani P, Platts A, Wang LL, Coon M, Nguyen T, Wang L, et al. A program for annotating and predicting the effects of single nucleotide polymorphisms, SnpEff: SNPs in the genome of *Drosophila melanogaster* strain w1118; iso-2; iso-3. *Fly (Austin).* 2012; 6: 80–92. <https://doi.org/10.4161/fly.19695> PMID: 22728672